IN VIVO AND *IN VITRO* DEGRADATION COMPARISON OF PURE MG, MG-10GD AND MG-2AG: A SHORT TERM STUDY

I. Marco[1,§,*], A. Myrissa[2,§], E. Martinelli[2], F. Feyerabend[3], R. Willumeit-Römer[3], A.M. Weinberg[2] and O. Van der Biest[1]

[1] Department of Materials Engineering, KU Leuven, Leuven, Belgium
[2] Department of Orthopaedic Surgery, Medical University Graz, Graz, Austria
[3] Institute of Materials Research, Helmholtz-Zentrum Geesthacht, Geesthacht, Germany

[§] These authors contributed equally

Abstract

The purpose of this study was to compare short term *in vitro* and *in vivo* biodegradation studies with low purity Mg (> 99.94 %), Mg-10Gd and Mg-2Ag designed for biodegradable implant applications. Three *in vitro* testing conditions were applied, using (i) phosphate buffered saline (PBS), (ii) Hank's balanced salt solution (HBSS) and (iii) Dulbecco's modified eagle medium (DMEM) in 5 % CO_2 under sterile conditions. Gas evolution and mass loss (ML) were assessed, as well as the degradation layer, by elemental mapping and scanning electron microscopy (SEM). *In vivo*, implantations were performed on male Sprague-Dawley rats evaluating both, gas cavity volume and implant volume reduction by micro-computed tomography (μCT), 7 d after implantation. Samples were produced by casting, solution heat treatment and extrusion in disc and pin shape for the *in vitro* and *in vivo* experiments, respectively. Results showed that when the processing of the Mg sample varied, differences were found not only in the alloy impurity content and the grain size, but also in the corrosion behaviour. An increase of Fe and Ni or a large grain size seemed to play a major role in the degradation process, while the influence of alloying elements, such as Gd and Ag, played a secondary role. Results also indicated that cell culture conditions induced degradation rates and degradation layer elemental composition comparable to *in vivo* conditions. These *in vitro* and *in vivo* degradation layers consisted of Mg hydroxide, Mg-Ca carbonate and Ca phosphate.

Keywords: Magnesium alloys, biodegradation, *in vitro*, *in vivo*, degradation.

*Address for correspondence:
Iñigo Marco
Department of Materials Engineering, KU Leuven
Kasteelpark Arenberg 44-bus 2450
3001 Leuven, Belgium
Telephone: +32 16373555
Fax: +32 16321990
Email: inigo.marco88@gmail.com

Introduction

Magnesium (Mg) is a promising material to be used during bone healing as biodegradable orthopaedic implant for fracture stabilisation. As a consequence of its degradability, the second surgery for implant removal can be avoided. Furthermore, Mg has similar density and mechanical properties compared to cortical bone, and has non-toxic and biocompatible properties as well (Kirkland *et al.*, 2010; Staiger *et al.*, 2006; Witte *et al.*, 2005). Complete bioresorption of Mg implants *in vivo* has been proven depending on the Mg-based material, keeping sufficient mechanical integrity during osteogenesis (Kraus *et al.*, 2012). Therefore, different applications can be aimed at by selecting the Mg alloy. Examples are bone fixation screws, intramedullary cavity fixation rod, cardiovascular stents, wound closing devices and scaffolds for tissue engineering.

However, biodegradation of pure Mg and Mg-alloys is a complex process, hard to predict. It is proven that ultrahigh-purity Mg degrades very slowly *in vitro* and *in vivo* with a degradation rate (DR) of 10 μm/year (Hofstetter *et al.*, 2015b). This shows the large influence of impurities on the biodegradation behaviour. Mg degradation is highly influenced not only by impurities (Hanawalt *et al.*, 1942; Hofstetter *et al.*, 2015a; Hofstetter *et al.*, 2015b; Lee *et al.*, 2009; Liu *et al.*, 2009; Reichek *et al.*, 1985; Yang *et al.*, 2015), but also by alloys addition and grain size (Liu *et al.*, 2015). Furthermore, the degradation conditions and the performance of the formed surface layer have also an impact (Walker *et al.*, 2012).

Although some attempts have been made to correlate *in vitro* and *in vivo* results (Li *et al.*, 2014; Li *et al.*, 2012; Shadanbaz *et al.*, 2014; Witte *et al.*, 2006), in general the comparison between different methods is poor (Martinez-Sanchez *et al.*, 2015). In some cases the immersion testing conditions apply different electrolytes, buffering and solution volume to sample surface ratio (V/S) and, as a result, the comparison with *in vivo* experiments is hardly possible (Li *et al.*, 2014). Hence, there is a need for a standardised *in vitro* testing method, which can be compared to *in vivo* conditions (Martinez-Sanchez *et al.*, 2015; Zhang *et al.*, 2013). For this reason we have selected three electrolytes, commonly used in literature, for an *in vitro* study: phosphate buffered saline (PBS) (Ahmadkhaniha *et al.*, 2016; Alvarez-Lopez *et al.*, 2010; Schille *et al.*, 2011; Trinidad *et al.*, 2013), Hank's balanced salt solution or Hank's solution (HBSS) (Wang *et al.*, 2008;

Zainal Abidin *et al.*, 2011) and a cell culture basal medium, Dulbecco's modified eagle medium (DMEM) (Feyerabend *et al.*, 2012; Marco *et al.*, 2016; Tie *et al.*, 2010; Tie *et al.*, 2013; Yang *et al.*, 2012), which is similar to plasma and whole blood (Feyerabend *et al.*, 2015). While PBS uses a phosphate ion based buffering system and DMEM contains a carbonate based system, HBSS contains a smaller amount of both buffering systems. Hofstetter *et al*. applied a setup with comparable *in vitro* and *in vivo* results, which consisted of one single stirred bath with the addition of CO_2 (Hofstetter *et al.*, 2015b). In the present work, cell culture conditions are applied with DMEM in a similar setup to that applied by Hofstetter *et al*. (2015b). The same testing conditions were also investigated in our previous work (Marco *et al*., 2016).

Since the required resorption rate for Mg-alloys depends on the application, different alloying elements, which can tune this rate, were selected. In the present study, the selected elements were silver (Ag) and gadolinium (Gd). Ag is considered as an impurity with a low tolerance limit, which accelerates the degradation process (Friedrich and Mordike, 2006). Moreover, Ag is known for its antibacterial properties (Tie *et al.*, 2013), also shown by Mg (Robinson *et al.*, 2010; Zhu *et al.*, 2014). Mg-Gd is reported as a slowly degrading alloy. Gd can form intermetallic compounds with impurities less harmful to the corrosion resistance (Mercer and Hillis, 1992) and it also improves the mechanical properties of Mg-Gd binary alloys (Hort *et al.*, 2010; Kubasek and Vojtech, 2013).

We analysed different Mg alloys, produced in disc and pin shape, under *in vitro* and *in vivo* conditions respectively, comparing DRs and surface layers formed after 7 d. In this analysis, impurity level and grain size were of great importance. Difficulties in distinguishing bone from the degradation layer after *in vivo* experiments by micro-computed tomography (μCT) have been recently reported (Galli *et al.*, 2015). These difficulties are related to the resolution of the tomographic method and the equipment used, and to differences in X-ray absorption between bone and the degradation layer. Therefore, this work also analyses the degradation layer trying to clarify the differences between bone and these layers and comparing the layers formed during *in vivo* and *in vitro* experiments.

Materials and Methods

Material preparation

The raw materials used for the Mg alloy production were magnesium (99.99 %, Xinxiang Jiuli Magnesium co. Ltd, Beijing, China), gadolinium (99.95 %, Grirem Adv. Mater. Co. Ltd., Beijing, China) and silver (99.99 %, ESG Edelmetall-Handel GmbH & Co. KG, Rheinstetten, Germany). All the alloys underwent thermomechanical processing steps at elevated temperatures appropriate for each alloy in order to homogenise their composition and microstructure. Ingots were cast in a permanent mould casting at 680-720 °C in protective atmosphere (Ar + 2 % SF_6) and heat treated for 6 h at 420-430 °C for Mg-2Ag and 500-550 °C for Mg-10Gd. Then Mg-10Gd and Mg-2Ag samples were extruded at 370-450 °C from a diameter of 30 mm to a diameter 12 mm with a speed of 2.5-4.5 mm/sec, while pure Mg was reduced in diameter from 110 mm to 12 mm at 300 °C at 0.7 mm/s without previous heat treatment. Finally, the wires were cut into discs of 10 mm diameter and 1.5 mm thickness, with a mass of approximately 180 mg each.

For the *in vivo* experiments, the same materials were used in pin shape and in order to achieve this, the extrusion was done to a final rod diameter of 6 mm. The extruded pure Mg (99.956 %) and Mg-10Gd rods (diameter = 6 mm) were further reduced to 1.6 mm diameter by turning (Ernst Wittner GmbH, Vienna, Austria). The Mg-2Ag extruded rods were drawn to wires using hardened steel drawplates. The wires were annealed at 300 °C for 45 min in the furnace applying 1 to 3 wire drawing steps and then they were drawn to a diameter of 1.6 mm. After production, the samples were sterilised by γ-irradiation at 29.2 kGy (BBF GmbH, Stuttgart, Germany) and afterwards, no surface preparation was applied.

Chemical composition and impurity content were determined by inductively coupled plasma optical emission spectroscopy (ICP-OES, Varian 720 ES, East Lyme, CT, USA). For grain size analysis, samples were embedded in epoxy resin and the surfaces prepared by grinding with SiC sandpaper of 1000-grits to 4000-grits (Matador 991A, Remscheid, Germany), and finally by polishing with diamond suspension of 3 μm (Kemet, Maidstone,

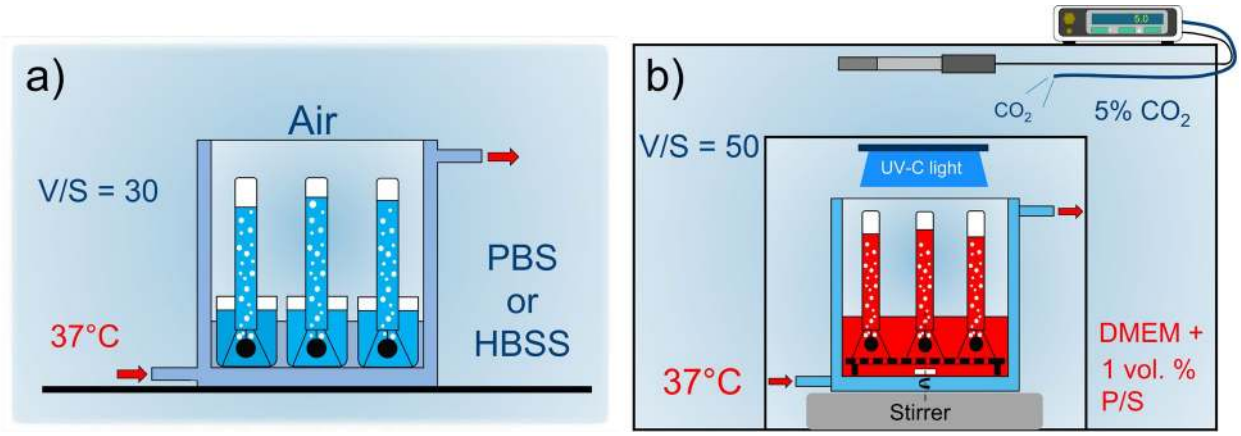

Fig. 1. Immersion test setups. (**a**) PBS and HBSS and (**b**) DMEM and 5 % CO_2 under sterile conditions. In DMEM, one single bath is stirred in order to assure the same pH and sterile conditions to the entire bath; in PBS and HBSS, the analysis is performed individually, since medium contamination does not occur.

Table 1. Ionic composition of different media used for Mg degradation tests in mmol/L.

	Na^+	K^+	Ca^{2+}	Mg^{2+}	Cl^-	HCO_3^-	$H_2PO_4^-$	HPO_4^{2-}	SO_4^{2-}	Amino acids	D-Glucose	Vitamins	Phenol red
PBS	154.1	4.1	-	-	140.6	-	1.5	8.1	-	-	-	-	-
HBSS	142.8	5.8	-	-	143.3	4.2	0.4	0.3	-	-	5.6	-	-
DMEM	155.3	5.3	1.8	0.8	115.7	44.1	-	0.9	0.8	10.6	25	0.15	0.04

England). Then, pure Mg- and Mg-10Gd-containing alloys were etched in picric acid solution (6 g of picric acid, 5 mL of acetic acid, 10 mL of H_2O and 100 mL of ethanol) for 2 s, while the etching of Mg-2Ag was done as quickly as manually possible (less than 1 s). Grain size was determined by optical microscopy and linear intercept method with ImageJ software (version 1.47v, Wayne Rasband, Bethesda, MD, USA). Density was measured with Archimedes's method comparing the mass of the samples in air and in ethanol at 25 °C.

In vitro degradation testing

For the *in vitro* degradation study, two different setup configurations were applied during 4 to 7 d (Fig. 1). On the one hand, PBS (4417, Sigma Aldrich, St. Louis, MO, USA) and HBSS (14175, Life Technologies, Grand Island, NY, USA) in atmosphere air at 37 ± 0.5 °C were used as non-physiological testing conditions (Fig. 1**a**). PBS and HBSS are electrolytes commonly applied in Mg degradation experiments as they have a strong buffering capacity, because they contain phosphates and, in HBSS case, also carbonates. On the other hand, testing under near physiological conditions or cell culture conditions (Fig. 1**b**) was performed as in our previous work (Marco *et al.*, 2016). This consisted of immersion in DMEM Glutamax-I (61965, Invitrogen, Paisley, UK) in air with 5 % CO_2 at 37 ± 0.5 °C with the same stirred bath of 600 mL under sterile conditions. In literature, it is recommended to apply one single bath for different physiological electrolyte concentrations (Hofstetter *et al.*, 2015b; Schinhammer *et al.*, 2013; Zainal Abidin *et al.*, 2013). However, for testing in PBS and HBSS each sample was immersed in one single bath to allow single pH measurements. In both configurations, experiments were performed simultaneously with six samples for each alloy. Table 1 shows the composition of the media used for the *in vitro* study.

The V/S ratio applied in this study was 30 mL/cm^2 for PBS and HBSS conditions and 50 mL/cm^2 for immersion in DMEM. As Kirkland *et al.* stated, at V/S ratios higher than 30 the V/S ratio has no longer a statistically significant influence on the DR (Kirkland *et al.*, 2012). The duration of the test depended on the limit of H_2 collection, which was defined by the eudiometer capacity of 35 mL, and the risk of DMEM contamination. As in our previous work, an empty control position test was performed without any sample under physiological conditions in order to evaluate the gas accumulation due to artefacts created by the stirring and the CO_2 in solution (Marco *et al.*, 2016).

The surface finishing of the discs was done firstly by grinding all the surfaces with SiC sandpaper of 1000-grits to 4000-grits (Matador 991A, Remscheid, Germany), and finally by polishing with diamond suspension of 3 µm (Kemet, Maidstone, England). The DRs were determined by mass loss (ML) measurements. Samples were first removed from the immersion bath and dried with hot air. Then they were immersed in a chromic acid [20 g chromium (VI) oxide (1257, Vel, Belgium), 1 g $AgNO_3$ (85228, Sigma Aldrich, Steinheim, Germany) and 100 mL distilled H_2O] for 30 min for the removal of the corrosion products. The DR was calculated in mm/year from the hydrogen generated and from the ML as indicated in equation 1 (1) and equation 2 (2), respectively. The gas volume, which was detected at the control position test, and the H_2 solubility in DMEM were corrected in order to calculate the DR by H_2.

$$DR = 87.6 \frac{P_{atm} V_{H2} M}{R T A t \rho} \quad (1)$$

where P_{atm} (1.013 atm) is the atmospheric pressure, H_2 volume corresponds to V_{H2} (mL), M is Mg molar mass (24.31 g × mol^{-1}), R is the ideal gas constant (0.082 atm × L × mol^{-1} × K^{-1}), T is the temperature (K), A is the sample area (cm^2), t is the immersion time (h) and ρ is the alloy density (g × cm^{-3}).

$$DR = 87600 \frac{\Delta W}{A t \rho} \quad (2)$$

where the mass difference between before testing and after chromic acid cleaning is ΔW (g).

In vivo experiments

All animal experiments were performed under ethical respect for animals and were authorised by the Austrian ministry of science and research (accreditation number BMWF-66.010/0078-II/3b/2011). 3 male Sprague-Dawley rats (n = 1 rat per group) of 150-170 g of weight and 5 weeks of age were used within this study. Cylindrical pins of 1.6 mm diameter and 8 mm length of pure Mg, Mg-10Gd and Mg-2Ag were used for the implantation. 2 pins of each alloy were implanted transcortically in the femoral bones of each rat. The entire implantation surgery took place under general anaesthesia and the postoperative treatment was described in detail by Kraus *et al.* (2012). µCT scans were performed with Siemens Inveon µCT (Knoxville, TN, USA) at day 1 and 7 after the operation. During the µCT scans, the animals were anaesthetised with volatile isoflurane (Forane#, Abbot AG, Baar, Switzerland). Siemens Inveon Acquisition Workplace 1.2.2.2 was the µCT scan software and scans of the rats were performed with a tungsten source at 70 kV voltage, 500 µA current and 1000 ms exposure time. The effective pixel size was

Table 2. Composition in weight percent (wt.%), impurity content in parts per million (ppm), grain size and density comparison of pure Mg, Mg-10Gd and Mg-2Ag in disc and pin shape. Fe, Ni and Cu impurity content was higher for pins than for discs due to the processing route and the lack of surface preparation.

		Gd wt.%	Ag wt.%	Fe ppm	Mn ppm	Si ppm	Ni ppm	Co ppm	Cu ppm	Al ppm	Mg wt.%	Grain size µm	Density g/cm³
pure Mg	disc	-	-	46	334	130	4	1	14	45	balance	22.6 ± 5.2	1.740
	pin	-	-	161	217	147	14	3	20	20	balance	18.3 ± 9.1	1.742
Mg-10Gd	disc	8.63	-	47	101	55	9	1	2	97	balance	17.8 ± 5.7	1.854
	pin	10.89	-	158	108	66	20	3	31	99	balance	19.9 ± 7.4	1.901
Mg-2Ag	disc	-	1.88	50	82	90	4	1	8	38	balance	43.7 ± 8.5	1.762
	pin	-	1.80	357	86	105	14	2	17	38	balance	25.6 ± 9.0	1.757

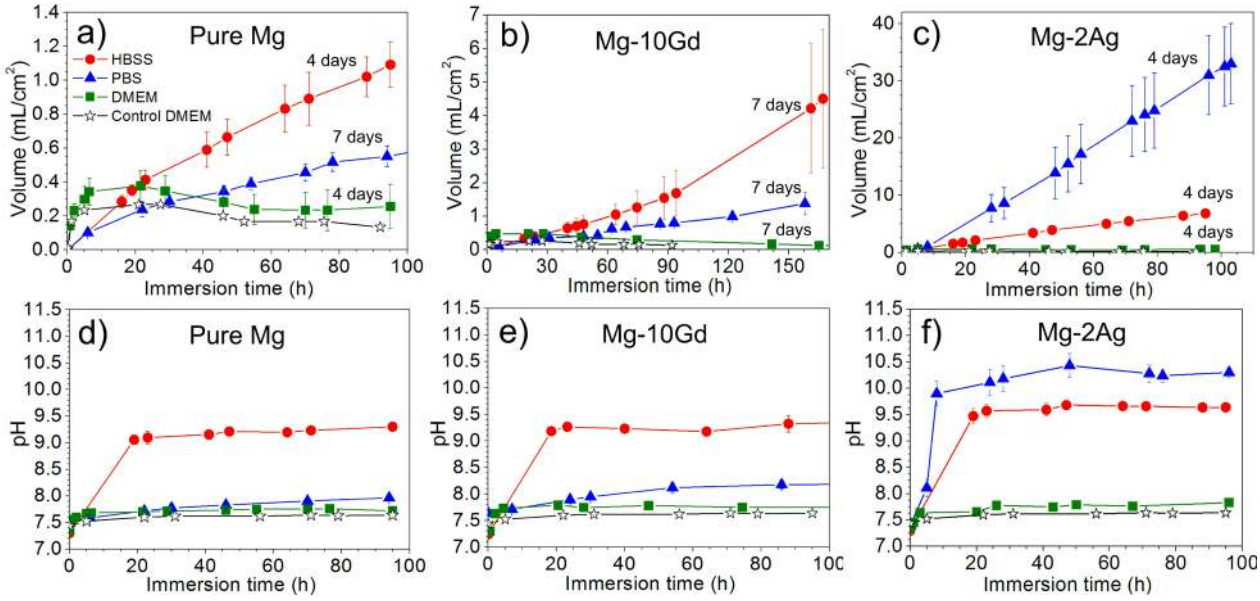

Fig. 2. Hydrogen evolution of (**a**) pure Mg, (**b**) Mg-10Gd and (**c**) Mg-2Ag, in PBS, HBSS and DMEM. pH evolution of (**d**) pure Mg, (**e**) Mg-10Gd and (**f**) Mg-2Ag in the same media for the first 100 h. Six samples were tested for each medium for 4-7 d; results are shown as means ± SD (standard deviation). The total duration of each test is indicated next to each H_2 evolution curve.

35.04 µm. An aluminium filter with a thickness of 0.5 mm was used. 3D morphometric analysis was executed and the pin volume and surface and gas volume were evaluated by using the Mimics software (Version 18.0, Materialise, Leuven, Belgium) as described by Kraus *et al.* (2012).

The DR ($n = 2$ bones per group) was calculated in mm/year during the 7 d after the operation by the equation 3:

$$DR_i = \frac{\Delta x_i}{\Delta t} \text{ with } \Delta x_i = \frac{\Delta V_i}{S_i} \quad (3)$$

where i is the observation time point, ΔV_i is the change of the volume between the observation time point i-1 and i (Δt) (mm³), S_i is the surface area at the observation time point i (mm²) and Δx_i is the degradation width (mm) (Fischerauer *et al.*, 2013). As mentioned above, the time points i are 1 and 7 d. Pin volume reduction was also calculated in percent during the 7 d after the operation.

Animals were euthanised 7 d after the operation as described in Kraus *et al.* (2012). Bones were explanted and directly frozen at −80 °C. Then they were sent, preserved with dry ice, to KU Leuven for the degradation layer analysis.

Degradation layer analysis

Both *in vitro* and *in vivo* tested samples were embedded in a high infiltration epoxy resin and after cutting and polishing, they were coated with platinum by sputtering to make the surface electrically conductive. Elemental mapping was performed with cross sections of tested samples using the Electron Probe Micro Analysis device (EPMA, JEOL Ltd. JXA-8530F, Akishima, Tokyo, Japan). All maps were acquired at 10 kV, 20 nA and 30 ms per dwell time, which is the acquisition time per pixel. Additionally, images were acquired by scanning electron microscopy (SEM, XL30 FEG, Philips, Eindhoven, The Netherlands) and elemental point analysis by energy dispersive X-ray spectroscopy (EDX, EDAX, Tilburg, The Netherlands). Elemental mapping analysis was also performed in other studies to characterise the degradation layer formed on Mg samples (Agha *et al.*, 2016; Willumeit *et al.*, 2011).

Results

Material characterisation

Table 2 shows the composition of the studied Mg alloys in disc and pin shape together with the impurity content of Fe, Mn, Si, Ni, Co, Cu and Al. The grain size and the alloy density are also included in Table 2.

Degradation tests

In vitro immersion tests

Fig. 2 shows the gas and pH evolution of pure Mg, Mg-10Gd and Mg-2Ag as function of time in PBS, HBSS and DMEM. Pure Mg and Mg-10Gd showed similar H_2 evolution curves in PBS and HBSS (Fig. 2**a**,**b**), although HBSS was slightly more aggressive than PBS to these two alloys. The pH was higher in HBSS (9-9.5) than in PBS (< 8.5) during the entire immersion time, demonstrating that HBSS had a weaker buffering power (Fig. 2**d-f**). Instead, Mg-2Ag had a higher H_2 evolution slope in PBS than in HBSS (Fig. 2**c**). The pH in this case was lower in PBS (9-9.5) than in HBSS (10-10.5) (Fig. 2**f**). Thus, a lower H_2 evolution slope corresponded to a lower DR and, consequently, a lower pH value was measured.

In DMEM the biodegradation process was slower for all three Mg based materials. A first gas increase was measured for the three materials during the first 10 h in DMEM reaching a maximum collected gas of 0.3-0.6 mL/cm^2 (Fig. 2). Then, the gas volume decreased during the rest of the immersion time with an approximate rate of 0.1 mL/cm^2/d. Within the position control test (without samples), a similar gas evolution was registered, but lower in volume, proving that some of the gas measured was CO_2 from the buffering system (Fig. 2**a**,**b**). Due to the nature of the biodegradation process of Mg, the rest must be H_2. The initial pH of DMEM was 7.4, but during testing the pH increased, getting stabilised at values between 7.7 and 7.9. The control position also revealed a pH of 7.6-7.7, which corresponded to the pH range of DMEM in 5 % CO_2. This indicated an increase of pH smaller than 0.3 between tests with and without Mg samples in DMEM. The fluctuation of the atmospheric pressure can also be a source of errors in the H_2 data recording, but it is considered the smallest

Table 3. DR of pure Mg, Mg-10Gd and Mg-2Ag in mm/year, calculated from the hydrogen collection and mass loss in PBS, HBSS, DMEM and by pin volume and surface *in vivo* at the end of each test.

		DR pure Mg [mm/year]	DR Mg-10Gd [mm/year]	DR Mg-2Ag [mm/year]
PBS	Mass loss	0.28 ± 0.07	0.61 ± 0.10	16.71 ± 3.06
PBS	Hydrogen	0.19 ± 0.02	0.40 ± 0.10	15.12 ± 2.97
HBSS	Mass loss	0.72 ± 0.31	1.57 ± 0.62	5.41 ± 0.71
HBSS	Hydrogen	0.57 ± 0.07	1.23 ± 0.56	3.48 ± 0.36
DMEM	Mass loss	1.07 ± 0.10	0.42 ± 0.12	2.21 ± 0.26
DMEM	Hydrogen	0.57 ± 0.07	0.20 ± 0.01	0.68 ± 0.04
In vivo	Pin volume and surface	0.15 ± 0.03	1.11 ± 0.05	0.13 ± 0.04

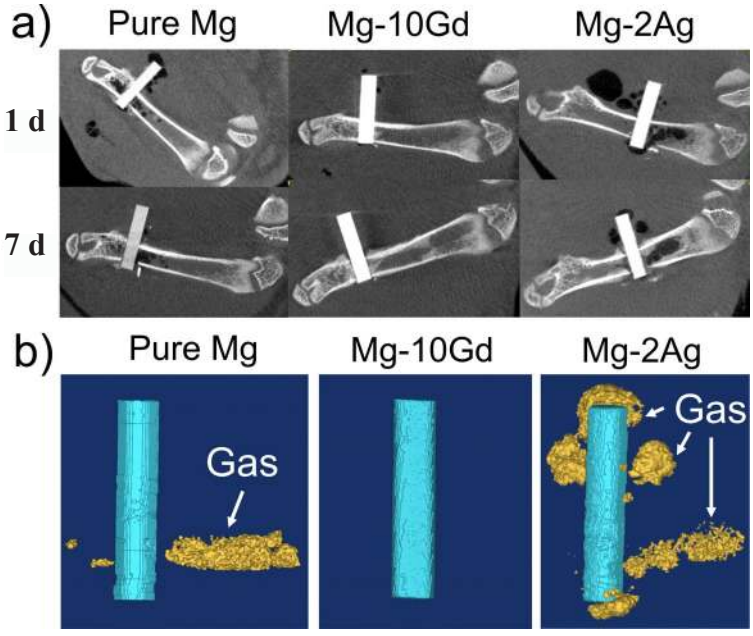

Fig. 3. (**a**) µCT scans of Sprague-Dawley rats implanted with Pure Mg, Mg-10Gd and Mg-2Ag alloys 1 and 7 d after the operation. The effective pixel size was 35 µm. (**b**) 3D reconstructed images of the different alloys with the surrounding gas release 7 d post-operative.

error, as shown by Hofstetter *et al.* (2015b). In Fig. 2, in some cases, the test was finished prematurely at day 4 for different reasons: (1) in PBS and HBSS, Mg-2Ag exceeded the limit of the gas storage capacity, (2) for pure Mg in PBS a linear behaviour was expected, as it was measured with Mg-10Gd, (3) in DMEM, the test with pure Mg and Mg-2Ag was interrupted due to risk of contamination by microorganisms after day 4, even though sterile conditions were equally applied in all the tests. This contamination was detected when the DMEM became turbid and the pH started to decrease.

In PBS and HBSS, severe localised and pitting corrosion could be observed on Mg-2Ag, while pure Mg and Mg-10Gd showed generally a homogeneous corrosion mode. A less aggressive degradation process was observed in DMEM. In this case, the degradation was homogeneous for every Mg-based material.

In vitro degradation rate

DRs were calculated starting from ML and hydrogen generation. DR results at the end of the immersion in each test condition are shown in Table 3. ML and H_2 methods correlated closely. DRs given by these two methods showed systematically higher values for ML than for H_2 evolution. According to the ML method, pure Mg degraded slower than 1.1 mm/year in every testing condition. Also, Mg-10Gd degraded at low DR in the three conditions. Finally, the DR of Mg-2Ag decreased from 16.7 mm/year in PBS to 5.4 mm/year in HBSS and 2.2 mm/year in DMEM. Thus, Mg-2Ag showed the highest DR in the three testing conditions compared to pure Mg and Mg-10Gd.

In vivo degradation rate

The µCT scans in Fig. 3 show the degradation performance after 7 d of implantation of pure Mg, Mg-10Gd and Mg-2Ag.

After 1 d of implantation, the µCT scan images with pure Mg showed gas formation in the intramedullary cavity around the implant as well as in the surrounding tissue. 7 d after the operation, the gas was localised only within the intramedullary cavity around the implant. 7 d after the implantation, the gas volume was 3.4 ± 1.93 mm^3 (Fig. 3**b**). Bone contact was observed since the first day due to the press fit implantation procedure of the pin.

In Mg-10Gd µCT scan images, very small pockets of gas bubbles were observed in the tissue surrounding the implant 1 d after the implantation. 7 d after the operation, the gas formation was not obvious and calculated to be

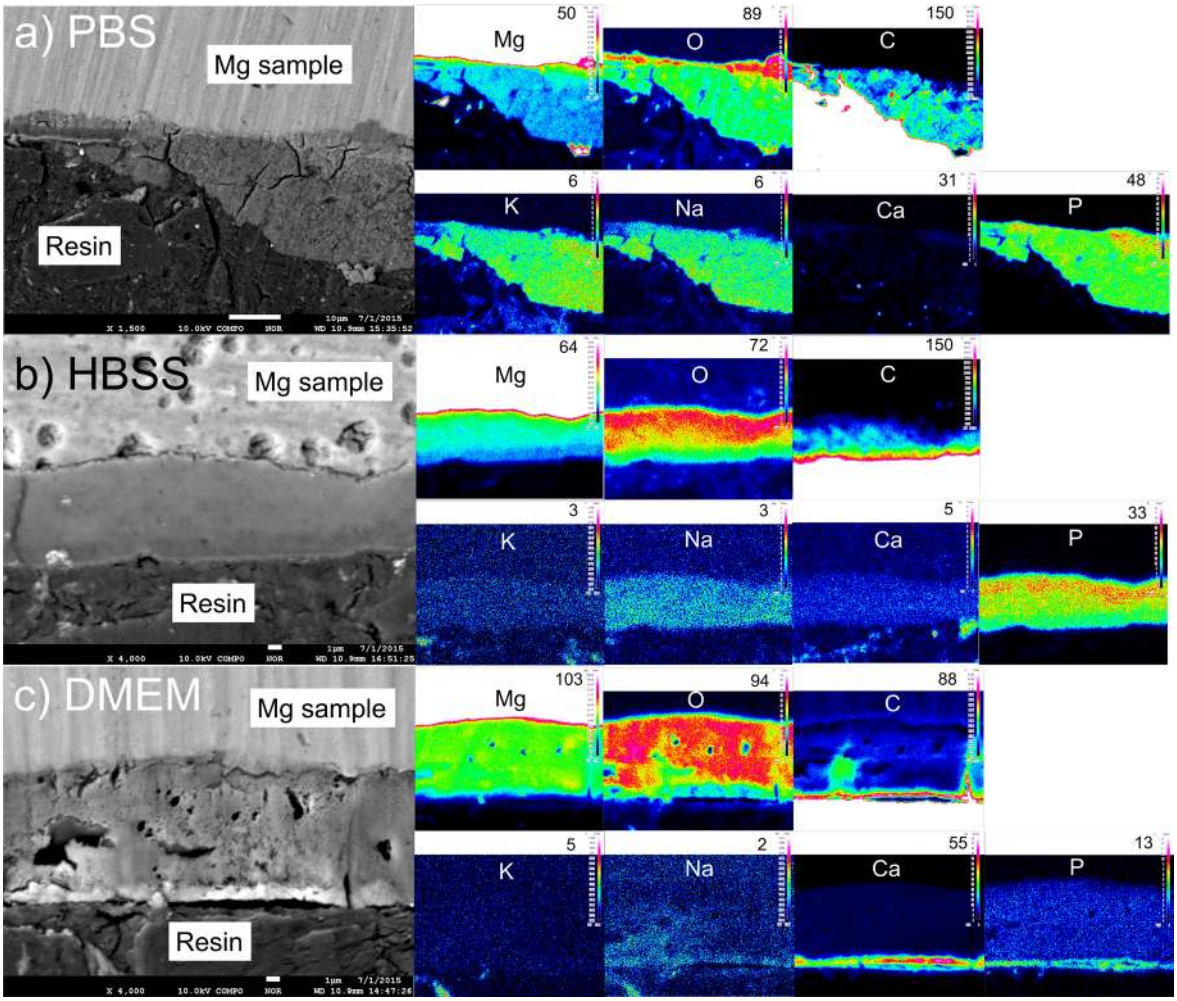

Fig. 4. Elemental mapping of the degradation layer formed on pure Mg samples immersed in (**a**) PBS, (**b**) HBSS and (**c**) DMEM for 7 d. The number on top of each picture indicates the maximum intensity on the scale bar. PBS maps were acquired with a resolution of 0.5 × 0.5 µm in approximately 75 min, while HBSS and DMEM maps were acquired in 1 h with a resolution of 0.1 × 0.1 µm.

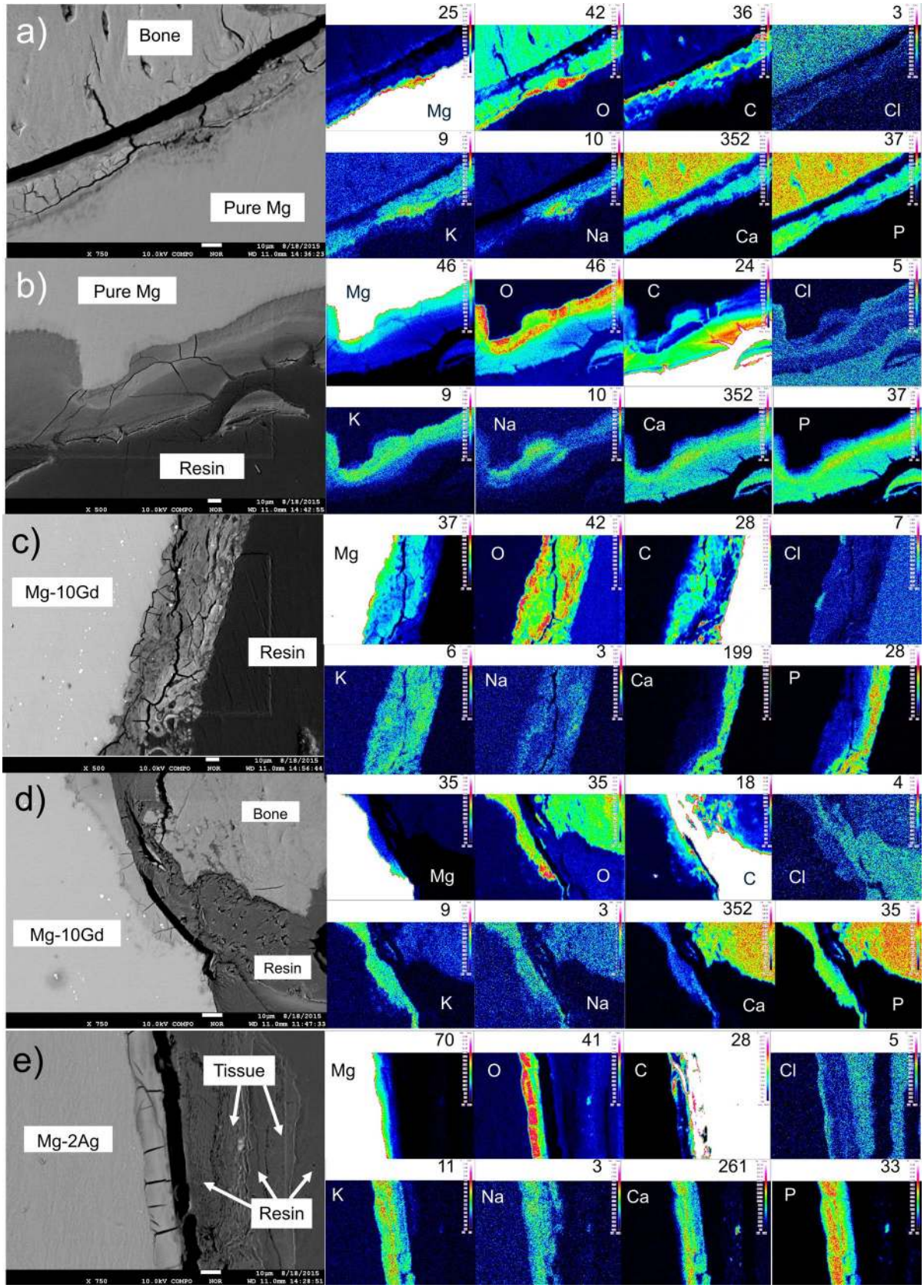

Fig. 5. Elemental mapping of the degradation layer formed on implanted pins after 7 d. Different sites on each Mg based material are analysed: (**a**) pure Mg in close contact with cortical bone; (**b**) pure Mg at the intramedullary cavity; (**c**) Mg-10Gd at the intramedullary cavity; (**d**) Mg-10Gd in the vicinity of the cortical bone; (**e**) Mg-2Ag at the intramedullary cavity. The elements mapped with different colour contrasts are Mg, O, C, Cl, K, Na, Ca and P. All maps were acquired with a resolution of 0.5 × 0.5 μm in approximately 75 min. The scale on the upper-right site of each elemental map is an approximation of the concentration of that element corresponding to the maximum of the scale bar. White scale bars at each SEM image correspond to 10 μm.

0.23 ± 0.32 mm^3 (Fig. 3**b**). In Mg-10Gd, the bone contact seemed to be tight since the first post-operative day, likely due to the press fit implantation of the pin.

1 d after implantation, Mg-2Ag μCT scan images showed a large amount of gas formation within the intramedullary cavity around the implant as well as in the surrounding tissue. 7 d after the operation, the gas bubbles were decreased in the surrounding tissue, but they were still present in the intramedullary cavity around the implant. The gas volume 7 d after the implantation was calculated to be 6.52 ± 8.41 mm^3 (Fig. 3**b**). Tight bone contact was also observed since the first day.

In vivo DRs, calculated from the pin volume loss and pin surface measured 7 d after implantation, are shown in Table 3. A smaller loss of pin volume was calculated for Mg and Mg-2Ag pins, which was comparable to the low DR of these materials in DMEM. A high DR of Mg-10Gd pin *in vivo* as compared to the low DR of Mg-10Gd discs in any *in vitro* immersion test was highlighted.

In all μCT images, no biodegradation was evident by visual examination alone, but slight pin volume reductions could be calculated using the Mimics software.

In vivo μCT results were used to examine bone growth and degradation behaviour, in order to provide proper information on volume and surface in the ongoing degradation process in the living animals. Unfortunately, a higher resolution and better contrast between degradation layer and bone was only possible after the explantation of the bone and the use of higher resolution *ex vivo* scanning protocols.

Degradation layers

In vitro

The degradation layers formed on pure Mg in PBS, HBSS and DMEM, analysed by elemental mapping, are shown in Fig. 4**a-c**. Mg-10Gd and Mg-2Ag are not shown because pure Mg represent closely the surface layers formed on these three electrolytes in the three condition.

In PBS, a layer containing Mg, O, P and C with traces of Na and K was identified (Fig. 4**a**). C was also present although PBS does not contain any C source. In HBSS, also Mg, O, P, C and traces of Na, K and Ca were detected (Fig. 4**b**): low O and high C levels were found on the outside of the degradation layer,while P level was high on the inner side of the degradation layer. In DMEM, the degradation layer contained different elements in two different regions, one rich in Mg, O and C and another one in P and Ca (Fig. 4c). In some cases there was a rim next to the Mg sample or the C containing resin which was an artefact caused by the large interaction volume of the beam.

In vivo

The degradation layers formed on pure Mg, Mg-10Gd and Mg-2Ag *in vivo* were characterised by elemental mapping (Fig. 5). Different layers were found *in vivo*, with different thickness and composition depending on the location (Fig. 6).Thus, two areas have been characterised for pure Mg and Mg-10Gd. Fig. 5**a** shows pure Mg in close contact with cortical bone. The elemental mapping indicated higher Ca and P levels in the bone compared to the degradation layer. Bone also contained traces of Cl. Sites rich in Mg and O were found in the area next to the Mg sample. Na and K were also incorporated in this layer. The C rich area highlighted the presence of biological entities. Fig. 5**b** shows a much thicker layer without bone contact. As a result, this region was more exposed to the environment and to the body fluid flow, which caused a faster degradation in this area. This faster degradation translated into a thicker surface film where clear differences in elemental content were distinguished. Conversely, Fig. 6**c** shows an exception to this observation, since there was a relatively thick layer on the Mg pin in contact with cortical bone, which presumably was related to a higher body fluid flow through this site. On the inner side, next to the Mg based material, were found higher levels of Mg and O compared to the outer side of the same layer. In this area also a higher K, Na and Cl and slightly higher Ca and P contents were detected. At the outer side, a higher C content was detected, which could indicate the presence of carbonate products. It is noteworthy that the resin applied for the sample preparation contained Cl, which could be confused with the Cl measured at the degradation layer, especially in such a low a concentration.

Fig. 5**c**,**d** depict the elemental mapping of the degradation layer formed on Mg-10Gd *in vivo*. Fig. 5**c** shows a region of the implant without bone contact. This area contains Mg, O, C, K, Ca and P homogeneously distributed and traces of Na and Cl. Ca and P were more intensely detected at the outer side of the rim, which can be commonly found along the surface layer. These Ca and P containing sites were also observed in Fig. 5**b**. Fig. 5**d** shows a region of the implant in the vicinity of the original femoral bone. Mainly Mg, O, C, Ca and P were found together with K and traces of Na and Cl. This layer on Mg-10Gd had no significant differences to the one observed on pure Mg in Fig. 5**a**,**b**. Moreover, similarly to Fig. 5**a**,**b**, a difference in Ca and P between bone and degradation layer was highlighted with, perhaps, a small change in the Cl content.

Finally, the elemental analysis of the degradation layer formed on Mg-2Ag at the medullary cavity is shown in Fig. 5**e**. On the one hand, Mg and O were homogeneously distributed, with a higher concentration in the inner part of the layer compared to the outer side. On the other hand, the C content varied substantially in different areas. The Cl content could indicate the presence of the resin. The observed concentration variations could be explained by the presence of tissue, since no bone was visible. Also, the Cl content might be slightly higher at the inner side of the degradation layer next to the Mg-2Ag implant, although the Cl concentration detected was rather low.

As shown in Fig. 6, the degradation layer thickness varied depending on the local environment where the sample was degrading. After 7 d of implantation, the thickness of the surface layer developed at the intramedullary cavity was 67.5 ± 19.4 μm (Fig. 6**b**) and at the outer part of the cortical femoral bone was 15.8 ± 3.3 μm (Fig. 6**a**). There were also differences at different implant-bone contact sites. Fig. 6**a**,**c** show two different sites where bone was in contact with the degradation layer. The degradation layer at the inner side of the cortical bone shown in Fig. 6**c** had a thickness of 40.9 μm.

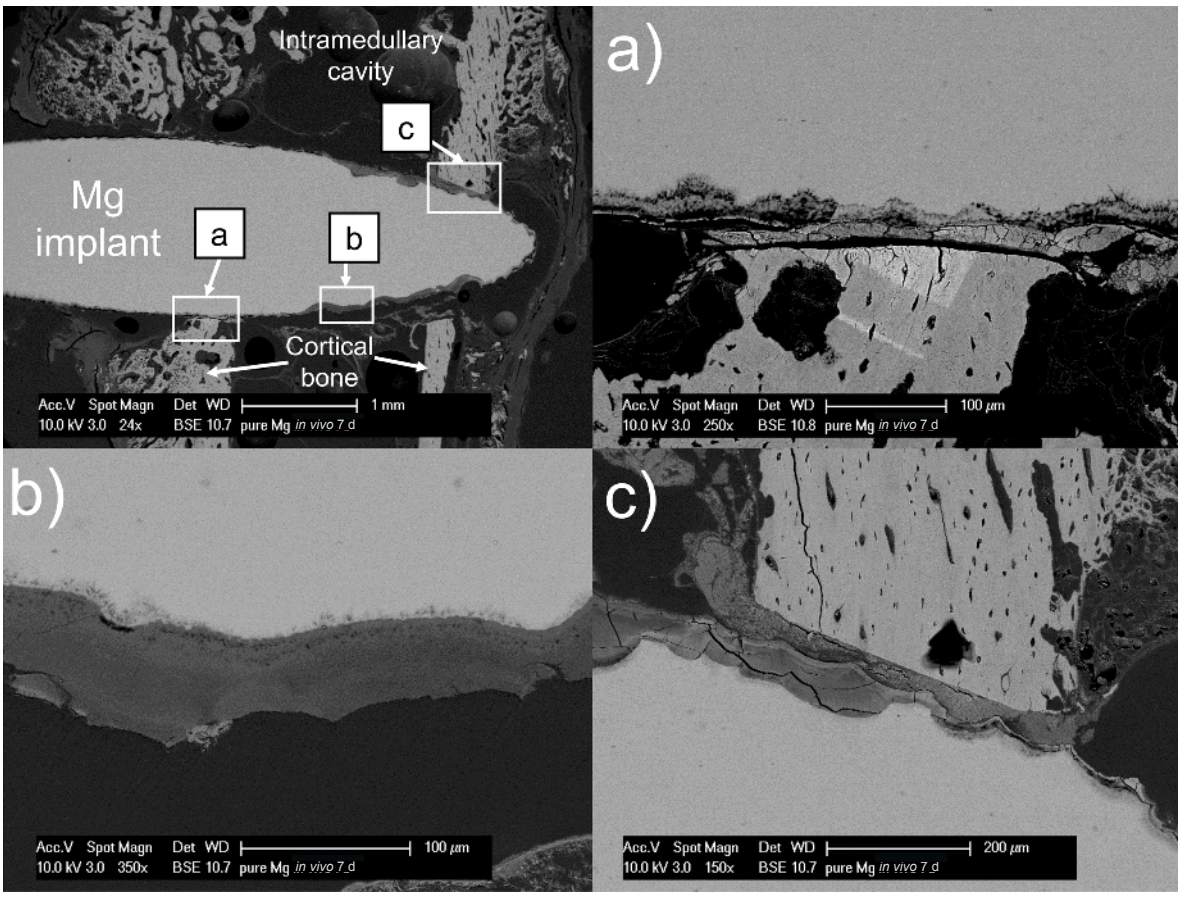

Fig. 6. SEM images of pure Mg implanted for 7 d show differences in degradation layer depending on the bone contact and the environment around the implant. (**a**) Slow degrading site characterised by a thin degradation layer deposition at an implant-bone contact site. (**b**) Thick degradation layer in the intramedullary cavity indicating a faster corrosion process. (**c**) Degradation layer at an implant-bone contact site, where a thicker layer related to a faster degradation process is observed. This is an exception to the observations from Fig. 5**b**,**c**, where a faster degradation was observed at the intramedullary cavity.

Initial surface

As shown in Fig. 7, the surface of the studied discs and pins has been analysed in order to determine the status of the surface before the immersion and *in vivo* tests, respectively. As mentioned above, discs have been ground and polished before *in vitro* immersion tests. The contact with air and moisture can generate a thin oxide film, which has been quantified by EDX in Fig. 7**a**. The O/Mg ratio can indicate the thickness of the oxide film. On the one hand, this O/Mg ratio for such polished samples was lower than 0.1, and on the other hand, pins which have been delivered, sterilised and stored for 1 to 2 years, showed a O/Mg ratio between 0.4 and 0.55. These oxides are also shown in Fig. 7**b** and can be identified as the grey areas on the pin surface. Fig. 7**b** closely represents the state of the surface finish of the Mg pins implanted. It has been recently proven that storage can have an influence on the degradation behaviour of Mg based materials; thus, while storing the material, a natural ageing process has been observed as well as an increase in oxygen-enriched regions on the implant surface (Bracht *et al.*, 2015). Thus, the pins are more oxidised compared to freshly ground discs applied in this study.

However, the thickness of this oxide layer was noticeably smaller than the degradation layer, due to the energy applied during the SEM (20 kV) and since Mg could still be detected through the greyish layer (see brighter areas within the grey areas in Fig. 7**b**). Thus, the thickness of the oxide layer was considered to be at least thinner than 1 µm, while the degradation layer will be thicker than 10 µm, in any case. Thus, the influence of this oxide layer is considered to be moderate.

Furthermore, as depicted in Fig.7**c**,**d**, impurity particles were also observed on the pin surface. These two images are examples of the many different impurity particles that could be found attached to the surface. The EDX spectrum from Fig. 7**c** shows clear Fe, Cr and Ni peaks, presumably indicating that these particles came from a stainless steel tool used for the extrusion or the machining. Fig. 7**d** shows another particle containing Cu and Zn, which might come from the original material or from contamination during casting, *i.e.* previous castings on the same permanent mould. Thus, the surface preparation (or the lack of it) might have an influence on the *in vivo* behaviour.

Discussion

Degradation layer

In PBS, the degradation layer was mainly formed by $Mg(OH)_2$ and Mg-PO_4 mixed in a non-distinguishable

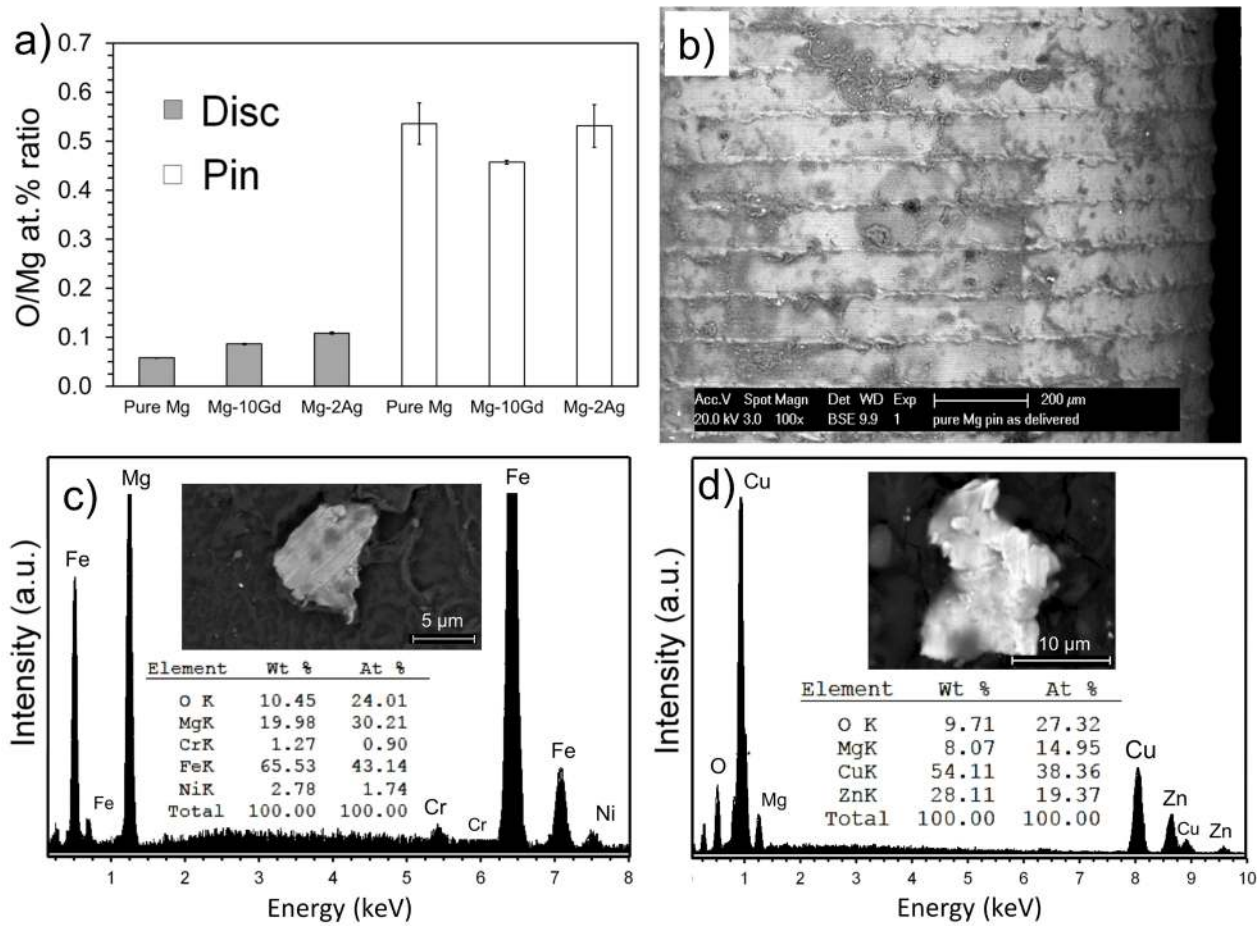

Fig. 7. Surface characterisation of the studied pins and discs tested. (**a**) Discs showed a lower oxidation level by EDX analysis compared to pins, which did not get any surface preparation. (**b**) Surface morphology in low magnification as an overview of the pin surface. The horizontal lines are machining marks due to turning. (**c**,**d**) Two impurity particles and their respective EDX point analysis. These particles came from the processing and the starting material.

manner due to a co-formation process (Fig. 3**a**). When the concentration of certain elements reaches the solubility limit, different compounds form the degradation layer. Moreover, in PBS, potassium phosphate can also nucleate on the surface and grow as a crystalline structure (Trinidad *et al.*, 2013). This phenomenon is explained by the large amount of phosphate ions present in PBS. It is possible that the C detected was an artefact of sample preparation, presumably due to a smearing effect of the resin. The degradation layer in PBS was generally non-uniform, with a changing thickness. In HBSS, the degradation layer was similar, with $Mg(OH)_2$ and $Mg\text{-}PO_4$ but also a small amount of $Mg\text{-}CO_3$ (Fig. 3**b**). In contrast to products formed in PBS, no potassium phosphate crystals were found due to the small amount of PO_4^{3-} in solution. Finally, as demonstrated in Fig. 3**c**, the degradation layer in DMEM was composed of two layers. As reported in our previous work (Marco *et al.*, 2016), the first one, next to the alloy surface, contained $Mg(OH)_2$ and $(Mg,Ca)\text{-}CO_3$. The second layer, on top of the first one, was a thin $(Mg,Ca)\text{-}PO_4$ layer, which was observed in Fig. 4**c**.

The degradation layer formed *in vivo* was comparable to the one observed in DMEM test condition. The detection of Mg and O indicated the presence of $Mg(OH)_2$; C indicated $(Mg,Ca)\text{-}CO_3$ and Ca and P indicated $Ca\text{-}PO_4$ corrosion products. Supporting this hypothesis, Yang and Zhang as well as Zong *et al.*, reported $Ca_3Mg_3(PO_4)_4$ to be present at the surface layer formed in Hanks solution by XRD (Yang and Zhang, 2009; Zong *et al.*, 2012). Hence, Ca-P layer might also include Mg in its structure, so that Ca-P can be defined as $(Mg,Ca)\text{-}PO_4$. The structure of this compound could be amorphous and further studies could clarify this matter. It was also possible to detect Na and K at a low concentration, which indicates that these two elements could also form phosphates or carbonates. The distribution of Na and K was homogeneous, meaning that these elements were distributed along the degradation layer by a co-formation process. Similarly to what was observed in DMEM (Fig. 3**c**), in animal experiments, Ca and P rich layers could also be formed separately from $Mg(OH)_2$ and $(Mg,Ca)\text{-}CO_3$ (Fig. 5**c**). Hence, this finding indicates the importance of the presence of Ca^{2+} and PO_4^{3-} ions in the electrolyte in order to allow calcium phosphate formation, which leads to a degradation layer in DMEM comparable to the one formed *in vivo* (Fig. 3**c** and Fig. 5). Some authors already reported the presence of these layers on Mg-based materials tested in HBSS (Kuwahara *et al.*, 2001; Yang and Zhang, 2009; Zong *et al.*, 2012), in DMEM (Willumeit *et al.*, 2011), in blood (Feyerabend *et al.*, 2015), in SBF (Zhang *et al.*, 2009) and in animal experiments (Li

et al., 2008; Xu *et al.*, 2007). Agha *et al*., recently showed the influence of different inorganic salts such as Ca^{2+}, SO_4^{2-} and HCO_3^-, present in cell culture media, on the Mg degradation process and the degradation layer formation (Ca-P and Mg-CO_3 products) (Agha *et al.*, 2016). This demonstrates that DMEM is a testing medium closer to a more realistic situation, when sterilisation is assured, in comparison to PBS and HBSS without Ca^{2+} also used in this study.

Along the surface layer formed *in vivo*, differences in thickness and composition can be found. Thus, it is difficult to identify one representative area of the whole degradation layer. These differences are caused by the environment in which the implant surface finds itself. Many influencing factors, such as bone contact, growth, fluid flow, its composition and biological content (*e.g.* osteoclasts and osteoblasts) can be measured.

It is also noteworthy that bone had higher Ca and P levels than the degradation layer, which could help to distinguish them (Fig. 5**a**,**d**). Thus, these Ca-P containing corrosion products have a different composition from hydroxyapatite, which is only composed of Ca, P and O (and traces of Cl) while the degradation layer also contains hydroxides and carbonates.

Degradation rate analysis

In vitro

In vitro and *in vivo* degradation behaviours of pure Mg, Mg-10Gd and Mg-2Ag, all in disc and pin shape, were compared during the first 7 d. Mg-2Ag discs showed the highest DR in the three *in vitro* testing conditions compared to pure Mg and Mg-10Gd. This could be explained by the presence of 1.88 wt.% (weight percent) of Ag, a larger grain size (43.7 μm) and large amount of Cl^- in PBS and HBSS. Ag is considered as an impurity, which accelerates the Mg degradation process (Friedrich and Mordike, 2006) by dissolving Mg around Ag-rich particles and releasing these particles. A greater Cl^- content in the electrolyte (*e.g.* in PBS and HBSS) will promote $Mg(OH)_2$ dissolution (Mueller *et al.*, 2009), exposing Mg and Ag and accelerating the degradation process even further. Therefore, the behaviour of Mg-2Ag in DMEM proved that testing in physiological conditions, *in vitro* leads to a less aggressive degradation process. Results from Mg-2Ag also indicate that a larger grain size also decreases the corrosion resistance of the Mg alloy (Liu *et al.*, 2015).

In contrast, pure Mg and Mg-10Gd in disc shape showed a stable and slow degradation compared to Mg-2Ag (Fig. 2 and Table 3). These two alloys have a smaller grain size (< 22.3 μm) and a larger amount of Mn. According to literature, Mn forms intermetallic particles with Fe, which are less favourable to promoting galvanic dissolution; thus, Mn increases the Fe tolerance limit (Lee *et al.*, 2009; Reichek *et al.*, 1985). Hence, Mn can reduce the negative influence of Fe on the corrosion behaviour, explaining the slower degradation behaviour of pure Mg and Mg-10Gd discs *in vitro*. The surface preparation of the discs facilitates the data interpretation since influencing parameter, such as impurities and oxidation at the sample surface, can be suppressed from the analysis. However, in a real application this preparation might not be possible.

There was a systematic difference between DRs calculated *in vitro* by gravimetry and by H_2 generation (Table 3). The H_2 evolution gave lower DR compared to the ML method. This difference can be explained by the particle undermining model (Song and Atrens, 1999), and perhaps the dissolution of hydrogen in the Mg sample (Atrens *et al.*, 2015; Remennik *et al.*, 2011; Zainal Abidin *et al.*, 2013).

In order to stabilise the pH within the physiological range (between 7 and 8), the use of DMEM buffered with CO_2 and HCO_3^- and the application of UV-C radiation for sterilisation seemed appropriate. Moreover, it mimicked the natural human blood buffering system. This allowed the presence of HCO_3^-, which is another important ion that promotes (Mg,Ca)-CO_3 formation at the surface layer. The stirring produced a dynamic flow making the sample and funnel an 'open' system avoiding a local pH increase inside the funnel, which falsifies the *in vitro* data, as other authors reported (Hofstetter *et al.*, 2015b; Kirkland *et al.*, 2012).

In summary, the PBS and HBSS with Ca^{2+} did not represent the degradation behaviour of Mg alloys *in vivo* because of the lack of relevant ions. This was indicated by the fast degradation of Mg-2Ag in PBS and HBSS, while its behaviour under near physiological conditions with DMEM and in animal experiments was rather stable.

In vivo

In degradation tests *in vivo*, the Mg-10Gd alloy, processed as a pin, had the highest DR in comparison to pure Mg and Mg-2Ag (Table 3). However, the number of gas pockets detected with Mg-10Gd was much lower than with pure Mg and Mg-2Ag (Fig. 3**b**). Many mechanisms can explain the lack of gas bubbles at the first stage of the degradation process of Mg implants. (i) Gas might not be trapped around the implant at this early healing stage. (ii) As Kuhlmann *et al.* reported, H_2 can be exchanged very quickly after implantation through tissue and skin (Kuhlmann *et al.*, 2013). (iii) Mg metal can store significant amounts of hydrogen (Nogita *et al.*, 2009). Many authors use the dissolution of hydrogen in the Mg sample to explain the difference between the DRs calculated by hydrogen evolution and by ML (Atrens *et al.*, 2015; Remennik *et al.*, 2011; Zainal Abidin *et al.*, 2013). (iv) Mg-RE alloys, *e.g.* Mg-10Gd, can form hydrides in cuboid shape absorbing hydrogen from the environment (Gan *et al.*, 2012; Marco *et al.*, 2016; Peng *et al.*, 2011). (v) Hydrogen might be incorporated in the degradation layer forming phosphate containing degradation products such as (Mg,Ca)-HPO_4 and (Mg,Ca)-$(H_2PO_4)_2$. Only the mechanisms (iv) can explain the lack of gas cavities around implanted Mg-10Gd pins. Perhaps mechanism (i) could also explain it, although the same procedure was applied during all the implantations.

If we compared the DRs *in vitro* with those *in vivo*, we observed that Mg-10Gd pins *in vivo* showed the highest DR while Mg-10Gd discs *in vitro* had the lowest DR, together with pure Mg (Table 3). This could be due to the large amount of Ni and Fe detected in Mg-10Gd pins (20 and 158 ppm, respectively). In this case, the larger amount of Ni and Fe contained in this alloy as a pin shape

indicated that the tolerance limits for these elements were exceeded, because Ni and Fe have the lowest tolerance limits (Hanawalt *et al.*, 1942). These impurities could originate from the initial material, or be added to the Mg alloy by contact with steel tools which can contain Fe, Ni and Cr as shown by the particle found on the surface in Fig. 7**c**. Thus, the processing route can have a large impact on the degradation performance of the Mg alloy. Moreover, these results indicated that the larger amount of Gd in pin shape compared to discs did not seem to play an important role in reducing the negative influence of impurities.

Interestingly, Mg-2Ag discs *in vitro* also showed the opposite behaviour to Mg-2Ag pins *in vivo* (Table 3). The larger grain size of discs (43.7 μm) *versus* pins (25.7 μm) did seem to increase the degradation process. However, in contrast with what is known, the larger amount of Fe content in Mg-2Ag pins (357 ppm) compared to discs (50 ppm) did not seem to increase the DR. There is a slower fluid flow restricted by bone and therefore, smaller amount of Cl^- ions in contact with the Mg-2Ag pins *in vivo*, which would accelerate the degradation process by the influence of Ag and Cl. In contrast, a large V/S ratio applied *in vitro* can explain the faster degradation of Mg-2Ag discs. In the literature, the use of a clinically relevant V/S ratio is recommended (Yang and Zhang, 2009; Zhen *et al.*, 2013). These degradation results from DMEM immersion *in vitro* tests and *in vivo* experiments (Table 3) are, especially in the case of Mg-2Ag, in accordance with a previous study where Mg-2Ag shows the highest DR in *in vitro* conditions in DMEM with 10 % of foetal bovine serum (FBS) (Myrissa *et al.*, 2016).

In general, these materials behaved in a different way under *in vivo* as compared to *in vitro* conditions. Firstly, this could be explained by the larger amount of impurities of Fe, Ni and Cu detected in the studied Mg pins as compared to discs. Mg-2Ag pins, for instance, had the greatest Fe content, which was due to a different processing with several more extrusion steps than pure Mg and Mg-10Gd pins. Moreover, the *in vivo* and *in vitro* tests applied, different conditions and many factors such as ion concentration, pH level or blood flow as well as protein and different kinds of cells can affect the DR of the materials (Martinez-Sanchez *et al.*, 2015; Mueller *et al.*, 2007; Poinern *et al.*, 2012; Shadanbaz *et al.*, 2014; Walker *et al.*, 2012; Witte *et al.*, 2006; Xue *et al.*, 2012; Yang *et al.*, 2012; Zainal Abidin *et al.*, 2013). Gas pockets were observed *in vivo*, which does not mean that bone is unable to heal completely ─ even if the resorption is too rapid and bubbles are large (Kraus *et al.*, 2012). In addition, the lack of surface preparation of the pins before implantation might have an influence since the oxide film can slow down the degradation process while the impurities might accelerate it. Although, the influence of the oxide layer is considered to be moderate, the complexity of the data interpretation does not increase in the case of neither polished nor ground pins.

Degradation mechanisms

In these short term studies the degradation mechanisms observed depended on the environment where the Mg sample was exposed. In general, under any testing condition, the Mg sample started degrading according to the following well-known anodic and cathodic reactions (equations 4 and 5, respectively).

$$Mg \rightarrow Mg^{2+} + 2e^- \quad (4)$$

$$2H_2O + 2e^- \rightarrow 2OH^- + H_2 \quad (5)$$

As explained above, a specific degradation layer was generated depending on the sample and the testing conditions applied to the Mg surface. Therefore, the degradation mode and the mechanisms depended on the degradation layer performance. During *in vivo* and *in vitro* tests with DMEM, homogeneous corrosion was observed on the studied Mg samples. Under these conditions, the degradation layer was formed by Ca and P rich layers separately from $Mg(OH)_2$ and (Mg,Ca)-CO_3. Therefore, these layers formed a more stable separation between the implant surface and the environment. This was also observed in DMEM in our previous work (Marco *et al*., 2016). A homogeneous degradation was also observed in PBS and HBSS with pure Mg and Mg-10Gd. Mg-2Ag, for instance, showed localised and pitting corrosion in PBS and HBSS due to the higher Cl^- content and the presence of Ag in the alloy. Hence, the degradation layer formed by $Mg(OH)_2$ and Mg-PO_4 did not protect the Mg surface in media with higher Cl^- ion content (> 140 mM).

Other mechanisms, such as particle undermining (Song and Atrens, 1999), could not be observed due to the short duration of these studies, although it was probably one of the factors influencing the lower DR calculated by hydrogen evolution as compared to the mass loss method. However, the influence of different impurity contents and oxidation of Mg surface still needs to be studied in a more systematic manner.

Conclusions

In vitro and *in vivo* degradation behaviour of several alloys was compared after 7 d. The degradation layer has been characterised in order to compare results from lab and animal studies. The results attested to the following:

The physiological testing set-up applied in this study, with DMEM as electrolyte, could not only maintain a physiological pH level, but also the degradation layer formed *in vivo* on several Mg alloys providing comparable DRs. These rates, especially for Mg-2Ag were lower in DMEM and *in vivo* than in PBS and HBSS. This indicates that *in vivo*, as well as *in vitro* under near physiological conditions, there were more moderate testing conditions that did not promote the Mg degradation process. The lower Cl^- ion concentration and the presence of Ca^{2+}, PO_4^{3-} and HCO_3^- ions highly influenced the degradation process of the studied Mg alloys and their consequent degradation layer formation. Hence, PBS and HBSS did not closely represent the degradation behaviour *in vivo*, because the degradation layer differed from what was found *in vivo*.

The same Mg alloy from another manufacturing process led to a different impurity content and microstructure,

which seemed to drive the degradation performance – downplaying the role of alloying additions, such as Gd and Ag. The importance of impurity and grain size control during the processing was thereby highlighted. The control of elements such as Fe and Ni, which have a low tolerance limit, must be reduced (to levels lower than 50 ppm and 10 ppm, respectively), but others, *e.g*. Mn, can be desirable when the purity is low.

The initial surface can contain impurity particles with Fe, Cu or Ni and an oxide layer as a result of the production process and the storage of the Mg implant. Therefore, a surface preparation was found recommendable in any Mg degradation study in order to facilitate data interpretation.

The elemental mapping revealed that hydroxyapatite in bone had higher Ca and P levels than the Ca-P rich degradation layer formed *in vivo*. Thus, these different calcium orthophosphate structures could help to distinguish bone from the degradation layer formed on the implant surface by elemental mapping.

Acknowledgements

This research is supported by the PEOPLE Programme (Marie Skłodowska-Curie Actions) of the European Union's Seventh Framework Programme FP7/2007-2013/ under REA grant agreement n˚289163. The authors also want to thank Gábor Szakács for all the work done in the material production, Johannes Eichler for the valuable help during the surgery and Claudia Kleinhans for the technical support. Furthermore, the authors appreciate the support of Prof. Ute Schäfer and they would like to thank the Institute of Biomedical Research at the Medical University of Graz for providing the infrastructure facilities to perform the animal studies.

We wish to confirm that there are no known conflicts of interest associated with this publication and there has been no significant financial support for this work that could have influenced its outcome.

References

Agha NA, Feyerabend F, Mihailova B, Heidrich S, Bismayer U, Willumeit-Römer R (2016) Magnesium degradation influenced by buffering salts in concentrations typical of *in vitro* and *in vivo* models. Mater Sci Eng C Mater Biol Appl **58**: 817-825.

Ahmadkhaniha D, Fedel M, Heydarzadeh Sohi M, Zarei Hanzaki A, Deflorian F (2016) Corrosion behavior of magnesium and magnesium-hydroxyapatite composite fabricated by friction stir processing in Dulbecco's phosphate buffered saline. Corros Sci **104**: 319-329.

Alvarez-Lopez M, Pereda MD, del Valle JA, Fernandez-Lorenzo M, Garcia-Alonso MC, Ruano OA, Escudero ML (2010) Corrosion behaviour of AZ31 magnesium alloy with different grain sizes in simulated biological fluids. Acta Biomater **6**: 1763-1771.

Atrens A, Song GL, Liu M, Shi Z, Cao F, Dargusch MS (2015) Review of recent developments in the field of magnesium corrosion. Adv Eng Mater **17**: 400-453.

Bracht K, Angrisani N, Seitz JM, Eifler R, Weizbauer A, Reifenrath J (2015) The influence of storage and heat treatment on a magnesium-based implant material: an *in vitro* and *in vivo* study. Biomed Eng Online **14**: 92.

Feyerabend F, Druecker H, Laipple D, Vogt C, Stekker M, Hort N, Willumeit R (2012) Ion release from magnesium materials in physiological solutions under different oxygen tensions. J Mate Sci Mater Med **23**: 9-24.

Feyerabend F, Wendel HP, Mihailova B, Heidrich S, Agha NA, Bismayer U, Willumeit-Römer R (2015) Blood compatibility of magnesium and its alloys. Acta Biomater **25**: 384-394.

Fischerauer SF, Kraus T, Wu X, Tangl S, Sorantin E, Hänzi AC, Löffler JF, Uggowitzer PJ, Weinberg AM (2013) *In vivo* degradation performance of micro-arc-oxidized magnesium implants: a micro-CT study in rats. Acta Biomater **9**: 5411-5420.

Friedrich HE, Mordike BL (2006) Magnesium technology. Springer-Verlag, Berlin: 470-481.

Galli S, Hammel JU, Herzen J, Szakács G, Lukáč F, Vlček M, Marco I, Wennerberg AM, Willumeit-Römer R, Jimbo R (2015) Corrosion behaviour of 3 Mg-alloys in bone: a high-resolution investigation. Eur Cell Mater **30 Supp 3**: 93.

Gan W, Huang Y, Yang L, Kainer KU, Jiang M, Brokmeier HG, Hort N (2012) Identification of unexpected hydrides in Mg-20 wt% Dy alloy by high-brilliance synchrotron radiation. J Appl Cryst **45**: 17-21.

Hanawalt J, Nelson C, Peloubet J (1942) Corrosion studies of magnesium and its alloys. AIME **147**: 273-299.

Hofstetter J, Martinelli E, Pogatscher S, Schmutz P, Povoden-Karadeniz E, Weinberg AM, Uggowitzer PJ, Löffler JF, (2015a) Influence of trace impurities on the *in vitro* and *in vivo* degradation of biodegradable Mg-5Zn-03Ca alloys. Acta Biomater **23**: 347-353.

Hofstetter J, Martinelli E, Weinberg AM, Becker M, Mingler B, Uggowitzer PJ, Löffler JF (2015b) Assessing the degradation performance of ultrahigh-purity magnesium *in vitro* and *in vivo*. Corros Sci **91**: 29-36.

Hort N, Huang Y, Fechner D, Stoermer M, Blawert C, Witte F, Vogt C, Druecker H, Willumeit R, Kainer KU, Feyerabend F (2010) Magnesium alloys as implant materials – principles of property design for Mg-RE alloys. Acta Biomater **6**: 1714-1725.

Kirkland NT, Birbilis N, Staiger MP (2012) Assessing the corrosion of biodegradable magnesium implants: a critical review of current methodologies and their limitations. Acta Biomater **8**: 925-936.

Kirkland NT, Lespagnol J, Birbilis N, Staiger MP (2010) A survey of bio-corrosion rates of magnesium alloys. Corros Sci **52**: 287-291.

Kraus T, Fischerauer SF, Hänzi AC, Uggowitzer PJ, Löffler JF, Weinberg AM (2012) Magnesium alloys for temporary implants in osteosynthesis: *In vivo* studies of their degradation and interaction with bone. Acta Biomater **8**: 1230-1238.

Kubasek J, Vojtech D (2013) Structural and corrosion characterisation of biodegradable Mg-RE (RE=Gd, Y, Nd) alloys. Trans Nonferrous Met Soc China **23**: 1215-1225.

Kuhlmann J, Bartsch I, Willbold E, Schuchardt S, Holz O, Hort N, Höche D, Heineman, WR, Witte F (2013) Fast

escape of hydrogen from gas cavities around corroding magnesium implants. Acta Biomater **9**: 8714-8721.

Kuwahara H, Al-Abdullat Y, Mazaki N, Tsutsumi S, Aisawa T (2001) Precipitation of magnesium apatite on pure magnesium surface during immersing in Hank's solution. Mater Trans **42**: 1317-1321.

Lee JY, Han G, Kim YC, Byun JY, Jang JI, Seok HK, Yang SJ (2009) Effects of impurities on the biodegradation behavior of pure magnesium. Met Mater Int **15**: 955-961.

Li H, Zheng Y, Qin L (2014) Progress of biodegradable metals Prog Nat Sci **24**: 414-422.

Li Y, Wen C, Mushahary D, Sravanthi R, Harishankar N, Pande G, Hodgson P (2012) Mg-Zr-Sr alloys as biodegradable implant materials. Acta Biomater **8**: 3177-3188.

Li Z, Gu X, Lou S, Zheng Y (2008) The development of binary Mg-Ca alloys for use as biodegradable materials within bone. Biomaterials **29**: 1329-1344.

Liu M, Uggowitzer PJ, Nagasekhar AV, Schmutz P, Easton M, Song GL, Atrens A (2009) Calculated phase diagrams and the corrosion of die-cast Mg-Al alloys. Corros Sci **51**: 602-619.

Liu Y, Liu D, You C, Chen M (2015) Effects of grain size on the corrosion resistance of pure magnesium by cooling rate-controlled solidification. Front Mater Sci **9**: 247-253.

Marco I, Feyerabend F, Willumeit-Römer R, Van der Biest O (2016) Degradation testing of Mg alloys in Dulbecco's modified eagle medium: influence of medium sterilisation. Mater Sci Eng C Mater Biol Appl: **62**: 68-78.

Martinez-Sanchez AH, Luthringer BJC, Feyerabend F, Willumeit R (2015) Mg and Mg alloys: how comparable are *in vitro* and *in vivo* corrosion rates? A review. Acta Biomater **13**: 16-31.

Mercer WE, Hillis JE (1992) The critical contaminant limits and salt water corrosion performance of magnesium AE42 Alloy. SAE, Detroit: 1-10.

Mueller WD, Fernandez-Lorenzo M, Nascimento ML, Zeddies M (2009) Degradation of magnesium and its alloys: dependence on the composition of the synthetic biological media. J Biomed Mater Res A **90**: 487-495.

Mueller WD, Nascimento ML, Zeddies M, Córsico M, Gassa LM, Fernandez Lorenzo de Mele M (2007) Magnesium and its alloys as degradable biomaterials: corrosion studies using potentiodynamic and EIS electrochemical techniques. Mater Res **10**: 5-10.

Myrissa A, Agha NA, Lu Y, Martinelli E, Eichler J, Szakács G, Kleinhans C, Willumeit-Römer R, Schäfer U, Weinberg AM (2016) *In vitro* and *in vivo* comparison of binary Mg alloys and pure Mg. Mater Sci Eng C Mater Biol Appl **61**: 865-874.

Nogita K, Ockert S, Pierce J, Greaves MC, Gourlay CM, Dahle AK (2009) Engineering the Mg-Mg_2Ni eutectic transformation to produce improved hydrogen storage alloys. Int J Hydrogen Energy **34**: 7686-7691.

Peng Q, Huang Y, Meng J, Li Y, Kainer KU (2011) Strain induced GdH_2 precipitate in Mg-Gd based alloys. Intermetallics **19**: 382-389.

Poinern GEJ, Brundavanam S, Fawcett D (2012) Biomedical magnesium alloys: a review of material properties, surface modifications and potential as a biodegradable orthopaedic implant. Am J Biomed Eng **2**: 218-240.

Reichek KN, Clark KJ, Hillis JE (1985) Controlling the salt water corrosion performance of magnesium AZ91 alloy. SAE transactions **94**: 318-329 doi:10.4271/850417.

Remennik S, Bartsch I, Willbold E, Witte F, Shechtman D (2011) New, fast corroding high ductility Mg-Bi-Ca and Mg-Bi-Si alloys, with no clinically observable gas formation in bone implants. Mater Sci Eng B Solid State Mater Adv Technol **176**: 1653-1659.

Robinson DA, Griffith RW, Shechtman D, Evans RB, Conzemius MG (2010) *In vitro* antibacterial properties of magnesium metal against *Escherichia coli*, *Pseudomonas aeruginosa* and *Staphylococcus aureus*. Acta Biomater **6**: 1869-1877.

Schille C, Braun M, Wendel HP, Scheideler L, Hort N, Reichel HP, Schweizer E, Geis-Gerstorfer J (2011) Corrosion of experimental magnesium alloys in blood and PBS: a gravimetric and microscopic evaluation. Mater Sci Eng B Solid State Mater Adv Technol **176**: 1797-1801.

Schinhammer M, Hofstetter J, Wegmann C, Moszner F, Loeffler JF, Uggowitzer PJ (2013) On the immersion testing of degradable implant materials in simulated body fluid: active pH regulation using CO_2. Adv Eng Mater **15**: 434-441.

Shadanbaz S, Walker J, Woodfield TB, Staiger MP, Dias GJ (2014) Monetite and brushite coated magnesium: *in vivo* and *in vitro* models for degradation analysis J Mater Sci Mater Med **25**: 173-183.

Song GL, Atrens A, (1999) Corrosion mechanisms of magnesium alloys. Adv Eng Mater **1**: 11-33.

Staiger MP, Pietak AM, Huadmai J, Dias G (2006) Magnesium and its alloys as orthopedic biomaterials: a review. Biomaterials **27**: 1728-1734.

Tie D, Feyerabend F, Hort N, Willumeit R, Hoeche D (2010) XPS studies of magnesium surfaces after exposure to Dulbecco's modified eagle medium, Hank's buffered salt solution, and simulated body fluid. Adv Eng Mater **12**: 699-704.

Tie D, Feyerabend F, Mueller WD, Schade R, Liefeith K, Kainer KU, Willumeit R (2013) Antibacterial biodegradable Mg-Ag alloys. Eur Cell Mater **25**: 284-298.

Trinidad J, Arruebarrena G, Marco I, Hurtado I, Saenz de Argandoña E (2013) Effectivity of fluoride treatment on hydrogen and corrosion product generation in temporal implants for different magnesium alloys. Proc Inst Mech Eng H **227**: 1301-1311.

Walker J, Shadanbaz S, Kirkland NT, Stace E, Woodfield T, Staiger MP, Dias GJ (2012) Magnesium alloys: predicting *in vivo* corrosion with *in vitro* immersion testing. J Biomed Mater Res B Appl Biomater **100**: 1134-1141.

Wang H, Estrin Y, Zúberová Z (2008) Bio-corrosion of a magnesium alloy with different processing histories. Mater Lett **62**: 2476-2479.

Willumeit R, Fischer J, Feyerabend F, Hort N, Bismayer U, Heidrich S, Mihailova B (2011) Chemical surface alteration of biodegradable magnesium exposed to corrosion media. Acta Biomater **7**: 2704-2715.

Witte F, Fischer J, Nellesen J, Crostack HA, Kaese V, Pisch A, Beckmann F, Windhagen H (2006) *In vitro* and *in vivo* corrosion measurements of magnesium alloys. Biomaterials **27**, 1013-1018.

Witte F, Kaese V, Haferkamp H, Switzer E, Meyer-Lindenberg A, Wirth CJ, Windhagen H (2005) *In vivo* corrosion of four magnesium alloys and the associated bone response. Biomaterials **26**: 287-291.

Xu L, Yu G, Zhang E, Pan F, Yang K (2007) *In vivo* corrosion behavior of Mg-Mn-Zn alloy for bone implant application. J Biomed Mater Res A **83**: 703-711.

Xue D, Yun Y, Tan Z, Dong Z, Schulz MJ (2012) *In vivo* and *in vitro* degradation behavior of magnesium alloys as biomaterials. J Mater Sci Techn **28**: 261-267.

Yang L, Hort N, Willumeit R, Feyerabend F, (2012) Effects of corrosion environment and proteins on magnesium corrosion. Corros Eng Sci Techn **47**: 335-339.

Yang L, Zhang E (2009) Biocorrosion behavior of magnesium alloy in different simulated fluids for biomedical application. Mater Sci Eng C Mater Biol Appl **29**: 1691-1696.

Yang L, Zhou X, Liang SM, Schmid-Fetzer R, Fan Z, Scamans G, Robson J, Thompson G (2015) Effect of traces of silicon on the formation of Fe-rich particles in pure magnesium and the corrosion susceptibility of magnesium. J Alloys Compd **619**: 396-400.

Zainal Abidin NI, Martin D, Atrens A (2011) Corrosion of high purity Mg, AZ91, ZE41 and Mg-2Zn-02Mn in Hank's solution at room temperature. Corros Sci **53**: 862-872.

Zainal Abidin NI, Rolfe B, Owen H, Malisano J, Martin D, Hofstetter J, Uggowitzer PJ, Atrens A (2013) The *in vivo* and *in vitro* corrosion of high-purity magnesium and magnesium alloys WZ21 and AZ91. Corros Sci **75**: 354-366.

Zhang LN, Hou ZT, Ye X, Xu ZB, Bai XL, Shang P (2013) The effect of selected alloying element additions on properties of Mg-based alloy as bioimplants: a literature review. Front. Mater. Sci. **7**: 227-236.

Zhang S, Li J, Song Y, Zhao C, Zhang X, Xie C, Zhang Y, Tao H, He Y, Jiang Y, Bian Y (2009) *In vitro* degradation, hemolysis and MC3T3-E1 cell adhesion of biodegradable Mg-Zn alloy. Mater Sci Eng C Mater Biol Appl **29**: 1907-1912.

Zhen Z, Xi TF, Zheng YF (2013) A review on *in vitro* corrosion performance test of biodegradable metallic materials. Trans Nonferrous Met Soc China **23**: 2283-2293.

Zhu L, Wan P, Duan J, Tan L, Yang K (2014) An alternative magnesium-based root canal disinfectant: preliminary study of its efficacy against *Enterococcus faecalis* and *Candida albicans in vitro*. Prog Nat Sci **24**: 441-445.

Zong Y, Yuan G, Zhang X, Mao L, Niu J, Ding W (2012) Comparison of biodegradable behaviors of AZ31 and Mg-Nd-Zn-Zr alloys in Hank's physiological solution. Mater Sci Eng B Solid State Mater Adv Technol **177**: 395-401.

Editor's note: There were no questions from reviewers for this paper, therefore there is no discussion with reviewers section.

Editor's note: The Scientific Editor responsible for this paper was Joost de Bruijn.